Dalton Transactions

ROYAL SOCIETY OF CHEMISTRY

PAPER

View Article Online
View Journal

Cite this: DOI: 10.1039/d5dt02909k

Spin dynamics and long phase-memory times in structurally distinct non-oxido vanadium(IV) complexes with rigid ligand frameworks relevant to molecular qubits

Oluseun Akintola, [a] Sudhir Lima,[a,b] Michael Seifert, [a] Benjamin Kintzel,[a] Helmar Görls,[a] Rupam Dinda *[b] and Winfried Plass *[a]

We report two chemically very similar non-oxido V(IV) complexes that feature distorted octahedral and distorted trigonal prismatic coordination geometries, as elucidated by single-crystal X-ray diffraction. Both compounds are thermally stable and show no degradation in the presence of air or water. An in-depth echo-detected field-sweep (EDFS) ESR spectroscopic study in frozen solution at temperatures below 10 K revealed resolved hyperfine interactions with the spin-bearing ^{51}V nucleus, along with additional couplings to neighboring ^{14}N and ^{1}H nuclei detected in ESEEM experiments. Investigation of the spin dynamics yielded long spin–lattice relaxation times (T_1) exceeding 100 ms at 5 K, which decreased to about 40 μs at 50 K. These long T_1 times therefore do not limit the spin coherence, and consequently the phase-memory times (T_m), at very low temperatures. The latter ranged from 5 to 8 μs and exhibited negligible temperature dependence within the investigated range. However, the use of a deuterated solvent increased T_m by approximately one order of magnitude to 52 μs at 5 K, though it also resulted in a more pronounced temperature dependence. Coherent spin manipulation was demonstrated by echo-detected transient nutation experiments, revealing well-defined Rabi oscillations with frequencies in the range of 13 MHz at an attenuation level of 9 dB and figures of merit exceeding 10^3 in deuterated solvent. Cluster correlation expansion (CCE) simulations reproduce the experimentally observed trends and identify the surrounding nuclear spin bath as the dominant decoherence source under dilution-limit conditions. No significant differences attributable to the distinct coordination geometries or structural variations in the ligand backbone were observed. These findings establish the present vanadium (IV) complexes as competitive candidates for molecular spin qubits and promising targets for future surface-deposition studies.

Received 4th December 2025,
Accepted 9th March 2026

DOI: 10.1039/d5dt02909k

rsc.li/dalton

Introduction

The foundation of quantum information processing lies in the fundamental concept of placing a quantum system in a superposition of states.[1] This remarkable property enables the realization of quantum bits (qubits), the basic units of quantum computation.[2] Among the various physical implementations of qubits, electronic spins are particularly appealing due to their intuitive nature and promising applications in diverse materials such as semiconductors[3] and quantum dots.[4]

Recently, molecular systems have emerged as viable qubit candidates. Organic radicals,[5] including nitroxyl radicals[6] and dithiolene complexes,[7] have demonstrated promising coherence properties. In particular, coordination complexes, and most notably oxidovanadium(IV) complexes, have attracted considerable attention due to their prolonged coherence times in the μs range.[8–13] To explore the influence of the oxido ligand, non-oxido vanadium(IV) complexes have also been investigated.[11,14–18] These systems have been shown to exhibit similarly long coherence times. Although in a vanadium(IV) dithiolate system the oxido form showed more favorable relaxation behavior,[10,17] the precise role of the vanadyl moiety in spin coherence remains unclear.[11] A general strategy to increase the coherence time of a given system is to embed qubits in a matrix free of nuclear spin, such as CS_2 or SO_2.[10,18] In cases where solubility prohibits such solvents, deuteration of the solvent can provide a viable alternative to prolong spin

[a]Institut für Anorganische und Analytische Chemie, Friedrich-Schiller-Universität, Jena, Humboldtstrasse 8, 07743 Jena, Germany. E-mail: sekr.plass@uni-jena.de; Fax: +49 (0)3641 948132; Tel: +49 (0)3641 948130
[b]Department of Chemistry, National Institute of Technology, Rourkela 769008, Odisha, India. E-mail: rupamdinda@nitrkl.ac.in

coherence times.[19] Notably, one such vanadium(IV) system based on a trisdithiolate coordination environment in CS_2 as a solvent achieved a spin-echo dephasing time (T_m) of up to 0.7 ms,[18] yet most reported phase-memory times fall in the range between 1 and 10 μs (see Table S1).[8,10–18,20–22]

Vanadium in its higher oxidation states (IV and V) is highly oxophilic and typically forms various oxido species, both in the solid state and in solution, characterized by strong terminal V=O bonds.[23,24] This tendency makes the isolation of non-oxido vanadium(IV) complexes particularly challenging, especially in aqueous media.[23,25] Although the naturally occurring non-oxido vanadium(IV) complex amavadin, an octa-coordinated species isolated from the mushroom Amanita muscaria,[26] demonstrates feasibility, the number of structurally characterized non-oxido vanadium(IV) complexes known today is still rather limited,[27–43] with the majority of these compounds featuring a six-coordinate environment.[27–40] Their formation is greatly facilitated by preorganized tridentate ligands, especially those with O/N/O[35–39] or O/N/S donor sets,[40] which contain at least one phenolic or alcoholic oxygen donor. These ligands are crucial in determining the coordination geometry (octahedral *vs.* trigonal prismatic),[27,30,36,44] the electronic ground state (d_{xy} *vs.* d_{z^2}),[44,45] isomerism (facial *vs.* meridional),[46] and thus the spectroscopic behavior of the complexes.[47]

In this report, we present the synthesis and characterization of two new aroylhydrazone-based non-oxido vanadium(IV) complexes with intermediate distortions between octahedral and trigonal prismatic coordination geometries. The spin coherence properties of these complexes in frozen solution were investigated. To eliminate the influence of spin–spin interactions, concentrations were deliberately kept low. Additionally, measurements were conducted in both protiated and deuterated solvents to probe the impact of nuclear-spin-driven decoherence arising from solvent protons.

Experimental section

Materials

All reagents and solvents used in the syntheses were of reagent grade and employed without further purification.

Methods

FT-IR spectra were measured on a VERTEX 70-IR spectrometer by Bruker Optics using the Specac Diamond ATR optional accessory. Mass spectrometry was performed on a MAT SSQ710 mass spectrometer made by Bruker. NMR spectra were recorded with an AVANCE 400 spectrometer from the same company. The elemental analysis was done on a VARIO EL III analyser. Simultaneous TG/DTA analyses were performed under static air atmosphere using a Netzsch STA Luxx PC analyzer up to 1000 °C.

Synthesis of ligands

An equimolar amount of *o*-vanillin (0.76 g, 5 mmol) and the corresponding hydrazide (5 mmol) was dissolved in ethanol (20 mL), and the resulting solution was refluxed for three hours. Upon cooling to room temperature, a precipitate was formed, which was filtered off, washed with ethanol, and dried over fused $CaCl_2$.

Synthesis of H_2L^1. Hydrazide used: 2-naphtho-hydrazide (0.93 g, 5 mmol). Yield: 1.44 g, 90%. ^{1}H NMR (400 MHz, dmso-d_6), δ (ppm): 12.25 (s, 1H, OH), 11.00 (s, 1H, NH), 8.72 (s, 1H, HC=N–), 6.89–8.58 (m, 10H, aromatic), 3.84 (s, 3H, CH_3–O). ^{13}C NMR (126 MHz, dmso-d_6), δ (ppm): 163.34, 148.60, 148.43, 147.64, 134.91, 132.54, 130.63, 129.42, 128.70, 128.61, 128.51, 128.20, 127.46, 124.69, 121.24, 119.55, 119.45, 114.29, 56.30. Selected IR data (ATR), $\tilde{\nu}_{max}$ (cm^{-1}): 1638, 1625, 1607, 1565, 1464, 1440, 1392, 1355, 1299, 1246, 1207, 1148, 1072, 960, 911, 872, 822, 776, 736, 693, 600, 520, 471.

Synthesis of H_2L^2. Hydrazide used: 3-hydroxy-2-naphtho-hydrazide (1.01 g, 5 mmol). Yield: 1.50 g, 89%. ^{1}H NMR (400 MHz, dmso-d_6), δ (ppm): 12.14 (s, 1H, OH), 11.27 (s, 1H, OH), 10.89 (s, 1H, NH), 8.70 (s, 1H, HC=N–), 6.89–8.46 (m, 9H, aromatic), 3.84 (s, 3H, CH_3–O). ^{13}C NMR (126 MHz, dmso-d_6), δ (ppm): 164.05, 154.50, 149.11, 148.44, 147.67, 136.36, 130.79, 129.14, 128.78, 127.23, 126.33, 124.32, 121.16, 120.53, 119.60, 119.37, 114.41, 111.03, 56.30. Selected IR data (ATR) $\tilde{\nu}_{max}$ (cm): 1622, 1608, 1556, 1547, 1516, 1468, 1451, 1359, 1344, 1256, 1219, 1168, 1099, 978, 880, 766, 728, 620, 606, 478, 445.

Synthesis of complexes

The complexes were prepared by adding [VO(acac)$_2$] (66 mg, 0.25 mmol) to a hot solution of the respective ligand H_2L^1 or H_2L^2 (2 equiv., 0.5 mmol) in acetonitrile (30 mL). The reaction mixture immediately turned dark green and was refluxed for 3 h. Upon standing at ambient conditions, dark green crystals formed, which were collected by filtration, washed several times with acetonitrile, and dried in air.

Synthesis of 1. Ligand used: H_2L^1 (160 mg, 0.5 mmol). Yield: 142 mg, 40%. Anal. calcd for **1**·0.5H_2O, $C_{38}H_{31}N_4O_{6.5}V$ (698.6 g mol^{-1}): C, 65.33; H, 4.47; N, 8.02. Found: C, 65.20; H, 4.04; N, 8.25. Selected IR data (ATR), $\tilde{\nu}_{max}$ (cm^{-1}): 1630, 1579, 1546, 1513, 1493, 1469, 1423, 1352, 1329, 1256, 1214, 1175, 1105, 1019, 982, 956, 937, 863, 824, 754, 736, 607, 474, 436.

Synthesis of 2. Ligand used: H_2L^2 (168 mg, 0.5 mmol). Yield: 160 mg, 44%. Anal. calcd for **2**·0.5H_2O, $C_{38}H_{31}N_4O_{8.5}V$ (730.6 g mol^{-1}): C, 62.47; H, 4.28; N, 7.67. Found: C, 62.93; H, 3.88; N, 7.84. Selected IR data (ATR), $\tilde{\nu}_{max}$ (cm^{-1}):1637, 1583, 1547, 1513, 1468, 1420, 1337, 1286, 1256, 1215, 1171, 1107, 972, 900, 870, 754, 732, 598, 522, 477, 448.

X-ray structure determination

The single crystal X-ray data for compounds **1** and **2** were collected on a Nonius KappaCCD diffractometer, using graphite-monochromated Mo-K_α radiation (λ = 0.71073 Å) at 133(2) K. Data were corrected for Lorentz and polarization effects, and absorption has been accounted for on a semi-empirical basis using multiple-scans.[48–50] The structures were solved by direct methods (SHELXS)[51] and refined by full-matrix least squares techniques against F_o^2 (SHELXL-2018).[52] All hydrogen atoms

were included at calculated positions with fixed thermal parameters. All non-hydrogen atoms were refined anisotropically. For disordered acetonitrile molecules in **2**, restraints on the distances and anisotropic displacement parameters were used (SAME and SIMU). Crystallographic data as well as structure solution and refinement details are summarized in Table S2. Diamond 5.1.0[53] was used for structure representations. Crystallographic data for the structures in this paper have been deposited with the CCDC 2506301 (**1**) and 2506302 (**2**).

Electron spin resonance spectroscopy

CW-EPR spectra were recorded in frozen solutions (1 mM) at 85 K using a Bruker ELEXSYS E580 X-band spectrometer equipped with an SHQE resonator (ER4122-SHQE) operating at 9.33 GHz. A microwave power of 0.47 mW was applied in 4 mm quartz tubes. Low temperatures were achieved using a quartz finger Dewar insert coupled to a Bruker ER4121 VT digital temperature controller. All simulations and fitting procedures were performed using EasySpin within the Matlab environment.[54] Data visualization was carried out using OriginPro 2024.[55] For pulsed ESR measurements, dilute solutions (*ca.* 0.1 mM) were prepared in chlorobenzene, both deuterated and non-deuterated. Samples in deuterated solvent are denoted as $\mathbf{1}^{D}$ and $\mathbf{2}^{D}$. Pulsed ESR experiments were carried out on a Bruker ELEXSYS E580 X-band spectrometer equipped with a FlexLine dielectric ring resonator (ER 4118 X-MD5, ν = 9.68 GHz). Temperatures between 5 and 50 K were controlled using an Oxford Instruments CF935 continuous-flow helium cryostat. Echo-detected field-sweep (EDFS) ESR spectra were recorded with the Hahn-echo pulse sequence ($\pi/2$–τ–π–τ–echo), using a fixed inter-pulse delay time τ = 200 ns and π and $\pi/2$ pulses of 32 and 16 ns, respectively. Spin–lattice relaxation times (T_1) were measured using the inversion recovery sequence (π–t_d–$\pi/2$–τ–π–τ–echo), with varying delay times (t_d) and fixed τ = 200, π = 32, and $\pi/2$ = 16 ns at the field of the most intense resonance in the EDFS spectra (346 mT). Phase-memory times (T_m) were measured by varying τ in the Hahn-echo sequence ($\pi/2$–τ–π–τ–echo) using pulse lengths of π = 32 and $\pi/2$ = 16 ns at the field of the most intense resonance in the EDFS spectra (346 mT). In contrast to the strictly defined transverse relaxation time T_2, which refers only to spin–spin interactions in the *xy*-plane, T_m provides a more comprehensive measure of decoherence, encompassing all processes that reduce echo coherence. ESEEM spectra were acquired using the three pulse sequence $\pi/2$–τ–$\pi/2$–T–$\pi/2$–τ–echo, with τ = 200, $\pi/2$ = 16 ns, and an initial delay time T of 300 ns with time increments of 8 ns. The raw time-domain ESEEM data were first baseline-corrected by fitting and subtracting a Gaussian envelope, then apodized with a Hamming window and zero-filled to improve digital resolution, and finally Fourier-transformed to produce the frequency-domain spectra. Echo-detected transient nutation experiments were performed at 5 K using the pulse sequence (t_p–T–π–τ–echo) with T = 800 ns and τ = 356 ns. The nutation pulse length t_p was incremented in steps of 2 ns starting from 0 ns. The π pulse length was adjusted according to the microwave attenuation level: 32 ns at 12 and 9 dB and 24 ns at 6 dB. Time-domain nutation data were phased to maximize the real signal component, baseline-corrected using a zero-order polynomial, zero-filled to four times the original length, apodized with a Hamming window, and Fourier transformed.

Cluster correlation expansion simulations

Cluster correlation expansion (CCE)[56] simulations were performed using the PyCCE package.[57] The simulation setup closely follows the methodology reported in ref. 58 for a related vanadium(IV) complex. The central spin system comprised the electron spin (S = 1/2) and the nuclear spin of vanadium. Simulations were carried out at a magnetic field of 0.33 T. Nuclear spin baths were modeled using hydrogen or deuterium densities of 2×10^{22} cm^{-3}. Electron spin baths were simulated at variable concentrations to estimate the dilution limit. The experimentally determined g and A tensors were used as input parameters. Convergence with respect to cluster order and bath cutoff radii was verified. Coherence functions were fitted using a stretched exponential function $L(t) = \exp[-(t/T_2)^{\beta}]$. Further computational details and convergence tests are provided in the SI.

Results and discussion

Syntheses

The two ligands $\mathbf{H_2L^1}$ and $\mathbf{H_2L^2}$ (see Scheme 1) were synthesized by refluxing equimolar amounts of 2-hydroxy-3-meth-

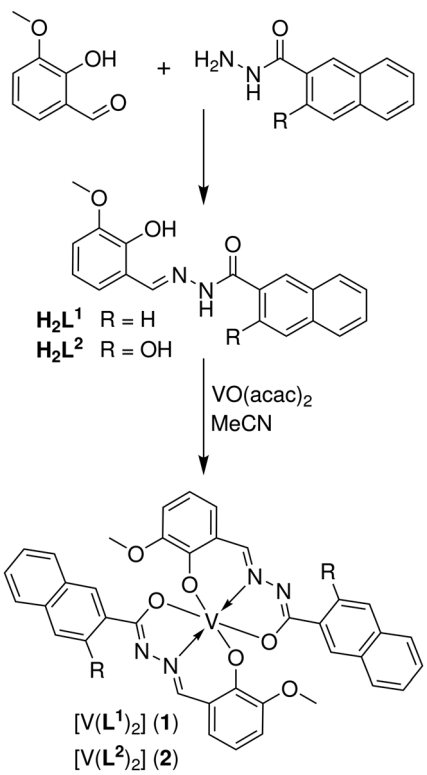

Scheme 1 Schematic representation of the complex syntheses.

oxybenzaldehyde with the appropriate hydrazide (2-naphthoic hydrazide for $\mathbf{H_2L^1}$ and 3-hydroxy-2-naphthoic hydrazide for $\mathbf{H_2L^2}$) in ethanol, following well-established literature procedures.[59,60] Both ligands were obtained in excellent yield, and their identity and purity were confirmed by ^{1}H and ^{13}C NMR spectroscopy.

The corresponding complexes **1** and **2** were prepared by dissolving the appropriate ligand and vanadyl acetylacetonate ([VO(acac)$_2$]) in a 2 : 1 molar ratio in hot acetonitrile and refluxing the mixture for 3 h (Scheme 1). Cooling the dark-green reaction mixtures to room temperature afforded dark-green crystals, which were isolated by filtration, washed thoroughly with acetonitrile, and air-dried. Elemental analyses agree with the proposed formulas, and thermogravimetric analysis of the complexes yield residual masses of 13.0 and 13.3%, in close agreement with the theoretical values of 12.5 and 13.0% for V_2O_5 as the final oxidative decomposition product. Further experimental and analytical details are provided in the Experimental section and Fig. S1.

X-ray crystal structures

Single crystals of **1** and **2** suitable for X-ray diffraction were obtained directly from the synthesis. Both crystallize in the triclinic space group $P\bar{1}$. **1** contains two independent complex molecules (**1A** and **1B**) in the asymmetric unit, each with one vanadium(IV) center, whereas the asymmetric unit of **2** contains a single independent molecule together with three acetonitrile solvent molecules, one of which is disordered over two positions in a 1 : 1 ratio. Selected crystallographic and refinement details are summarized in Table S2.

In all complex molecules of **1** and **2**, the vanadium(IV) centers are six-coordinate, each coordinated by two crystallographically independent dianionic ligands. The V–O (180–198 pm) and V–N (206–210 pm) bond lengths in **1A**, **1B**, and 2 fall within typical ranges for non-oxido vanadium(IV) complexes (Table S3), and bond valence sums of 4.02, 4.15 and 4.18 confirm the +IV oxidation state.[61] The structures of the complex molecules **1A**, **1B**, and **2** are depicted in Fig. 1 and 2.

Non-oxido vanadium(IV) complexes with tridentate hydrazone-based ligands generally adopt six-coordinate geometries between the ideal octahedral and trigonal-prismatic limits. The concept of continuous shape measures (CShM)[62] quantifies deviations from these reference polyhedra *via* the structural descriptors S(OC-6) and S(TRP-6) ($0 \leq S \leq 100$, where 0 represents the perfect match). According to CShM analyses, most reported non-oxido vanadium(IV) complexes with hydrazone-based ligands cluster near either the trigonal-prismatic (S(TRP-6) < 2) or octahedral (S(OC-6) ≈ 2) limits, while only few examples occupy an intermediate region, which is expanded by the new complexes **1** and **2** (Table S3). The two independent molecules of **1** display distorted octahedral coordination environments (S(OC-6) ≈ 3.6, S(TRP-6) ≈ 7.9), whereas **2** adopts a clearly intermediate geometry (S(OC-6) = 5.74, S (TRP-6) = 4.58).

An alternative approach for structural analysis employs the angular descriptors Θ and Ω, defined as the mean twist angle between opposite triangular faces (Θ) and the donor–V–donor angle between the terminal donor atoms of the two tridentate ligands (Ω).[47] In this description, the octahedral and trigonal-prismatic limits correspond to Θ = 60°, Ω = 180° and Θ = 0°, Ω = 90°, respectively. These descriptors are in good agreement with the CShM results (Table S3). However, the rigidity of tridentate aroylhydrazone ligands imposes limitations, particularly on Ω, which in literature-known examples ranges from 125 to 160°, thus remaining well away from the ideal limits. In contrast, the twist angles Θ are much closer to the theoretical range, spanning from 1 to 48°. For both **1** and **2**, the angular parameters Θ and Ω consistently indicate an essentially intermediate coordination geometry between the octahedral and trigonal-prismatic limits, confirming that the present aroylhydrazone ligands populate the region between the idealized extremes. Other tridentate ligand systems, however, can approach the octahedral[34,46] and trigonal-prismatic[45,63,64] limits much more closely in terms of Ω.

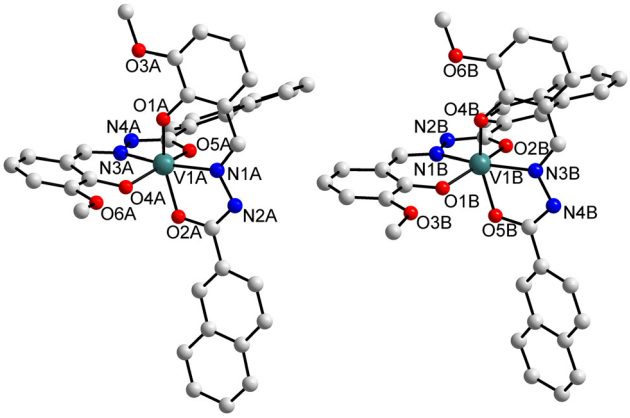

Fig. 1 Structures of both independent complex molecules present in asymmetric unit of **1**. Hydrogen atoms have been omitted for clarity.

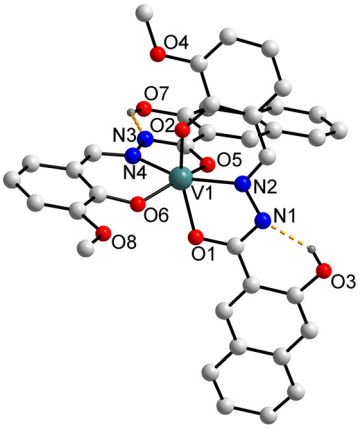

Fig. 2 Molecular structure of **2**. Solvent molecules and hydrogen atoms not participating in hydrogen bonding have been omitted for clarity.

The core of the deprotonated aroylhydrazone ligands (Scheme 1), which defines the tridentate coordination pocket, is π-conjugated and therefore essentially planar in the complex molecules, with the vanadium(IV) centers displaced from the mean ligand planes by 22–41 pm. In contrast, the naphthyl substituent at the acyl carbon atom of the aroylhydrazone ligands retains rotational freedom, resulting in N–C–C–C(R) torsion angles (Scheme 1) of 8–25° in **1**. For **2**, the corresponding torsion is significantly smaller (1–6°), which can be attributed to intramolecular hydrogen bonding, with O3···N1 and O7···N3 distances of 257 and 267, pm, respectively.

The packing in the crystal structures of both complexes **1** and **2** is characterized by π interactions involving naphthyl and phenyl groups as well as the central π-conjugated hydrazide moiety of the ligands, as depicted in Fig. S2–S5.

For complex **1**, interactions between naphthyl groups of the two independent molecules and the hydrazide group of one ligand at V1B results in the formation of a chain-like association of the two independent complex molecules **1A** and **1B** along the crystallographic [001] direction (Fig. S3). The combination of these weak π interactions with steric effects from neighboring molecules in the packing can explain the observed variation in the twist between the naphthyl substituent and the remaining aroylhydrazone moiety of the ligands.

In contrast, the crystal packing of **2** is dominated by stronger π–π interactions. The shortest mean-plane distances are found for interactions between the π-conjugated hydrazide moieties of ligands containing the nitrogen atoms N1 and N2 of neighboring complex molecules (320 pm), leading to the formation of dimers (red dashed lines in Fig. S5). π interactions involving hydrazide groups have also been reported for related organic molecules[65] and complexes.[66] These dimers are further connected *via* π–π interactions between neighboring complex molecules, either involving the methoxy-salicylidene moiety (blue dashed lines in Fig. S5) or the naphthyl-carboxylic acid hydrazide moiety (orange dashed lines in Fig. S5) of the second ligand containing the nitrogen atoms N3 and N4, thereby forming a three-dimensional network. The comparatively strong π interactions found in the crystal packing of **2** are facilitated by the hydroxy substituent at the naphthyl group, which enforces planarity relative to the remaining aroylhydrazone part of the ligand. Interestingly, the 3D network formed leads to solvent-accessible channels filled with additional acetonitrile molecules (see Fig. S4). These channels run along the [100] and [010] directions at the unit cell faces (*i.e.*, $y = 0$ and $z = 1/2$ as well as $y = 1$ and $z = 1/2$) and the unit cell center (*i.e.*, $x = 1/2$ and $z = 1/2$), respectively.

Continuous-wave and echo-detected field-sweep ESR spectra

Continuous-wave (CW) X-band ESR spectra of the complexes **1** and **2** were recorded on frozen solutions in both the protiated and deuterated forms of chlorobenzene (see Fig. 3) to investigate their spin-Hamiltonian parameters. The spectra were satisfactorily reproduced using an effective spin Hamiltonian (see eqn (1)) comprising a rhombic *g* tensor and rhombic hyperfine

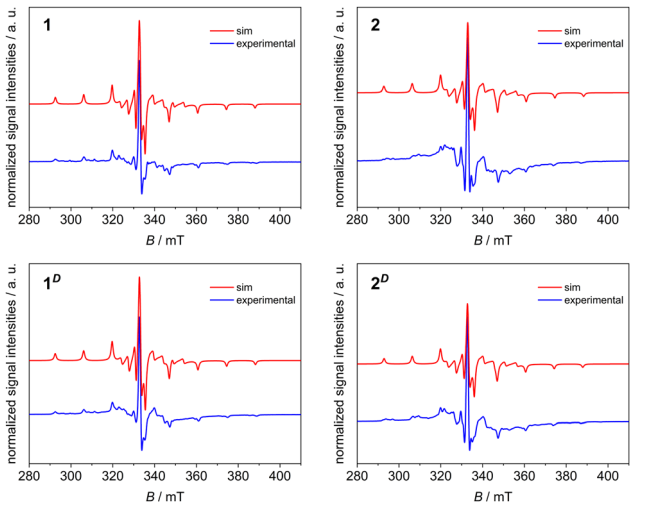

Fig. 3 CW X-band ESR spectra of **1** (left) and **2** (right) recorded in protiated (top) and deuterated (bottom) chlorobenzene at 85 K. Experimental data are shown in blue (lower trace) and fits in red (upper trace).

coupling to the ^{51}V nucleus, with the fitted parameters summarized in Table 1.

$$\hat{H}_{spin} = \mu_B \mathbf{B} \cdot \mathbf{g} \cdot \hat{\mathbf{S}} + \hat{\mathbf{S}} \cdot \mathbf{A} \cdot \hat{\mathbf{I}} - \mu_N \mathbf{B} \cdot \mathbf{g}_N \cdot \hat{\mathbf{I}} \quad (1)$$

In addition to the CW measurements, echo-detected field-sweep (EDFS) ESR spectra were recorded using the standard Hahn-echo pulse sequence for **1** and **2** (Fig. S6). The observation of a spin echo is a first indication that quantum coherence is observed in these samples. For the simulation of the EDFS spectra, the spin-Hamiltonian parameters derived from the CW spectrum were employed yielding good agreement with experiment and confirming that the coherent signal originates from the entire sample. A weak additional contribution is visible in the region of the parallel hyperfine structure, which may originate from a minor species, possibly related to different conformers present in the frozen solution.

For both **1** and **2**, the obtained *g* values reveal a rhombic *g* tensor with rhombicity parameters η_g of 0.032 and 0.161, respectively. Interestingly, the hyperfine coupling tensor *A*

Table 1 Parameters obtained from simulation of CW X-band ESR spectra of **1** and **2** recorded in protiated (PhCl) and deuterated chlorobenzene (PhCl-d_5); measurements in the deuterated solvent are indicated by the superscript *D*

	1	**2**	**1**^{D}	**2**^{D}
g_1	1.958	1.957	1.958	1.957
g_2	1.963	1.958	1.963	1.958
g_3	1.989	1.988	1.989	1.988
Linewidth (mT)	1.2	1.3	1.2	1.3
A_1 (MHz)	374	374	375	372
A_2 (MHz)	119	129	116	129
A_3 (MHz)	20	29	24	28

exhibits significant rhombicity. These observations are consistent with the distorted coordination environment of the complexes **1** and **2**, which are intermediate between octahedral and trigonal-prismatic geometries (see Table S5). It is important to note that the structural metrics are derived from solid-state crystallography, whereas the CW ESR spectra were recorded on frozen solutions. This means that subtle structural rearrangements upon dissolution and vitrification cannot be excluded.

Comparison with structurally and spectroscopically characterized non-oxido vanadium(IV) complexes featuring tridentate hydrazone-based ligands (summarized in Table S5) reveals that systems closer to octahedral coordination typically exhibit a prolate *g* tensor, whereas those approaching trigonal-prismatic geometry predominantly display an oblate anisotropy. This overall trend is consistent with ligand-field considerations for d^1 ions.[67]

In ideal or weakly distorted octahedral environments, axial elongation stabilizes the d_{z^2} orbital, resulting in a singly occupied molecular orbital (SOMO) with dominant d_{z^2} character. For a pure d_{z^2} ground state the orbital angular momentum along the molecular *z* axis vanishes ($L_z|d_{z^2}\rangle = 0$), so that spin–orbit coupling does not contribute significantly to the $g_\parallel$ component. Consequently, $g_\parallel$ remains close to the free-electron value g_e, while the largest deviations from g_e arise for the perpendicular components through mixing with excited states *via* the L_x and L_y operators. This situation typically results in a prolate *g* tensor ($g_\parallel > g_\perp$). The experimentally observed value of $g_\parallel$ slightly below g_e indicates a minor admixture of $d_{x^2-y^2}$ character into the ground state. Conversely, in trigonal-prismatic coordination environments the SOMO is, in the idealized D_{3h} limit, derived mainly from the *e′* set ($d_{x^2-y^2}$, d_{xy}), *i.e.*, orbitals oriented within the basal plane. In this case, spin–orbit coupling most effectively mixes the ground state with excited states through the L_z operator, leading to the largest deviation of $g_\parallel$ from g_e. As a consequence, such systems typically display an oblate *g* tensor ($g_\perp > g_\parallel$).

However, as also evident from the data compiled in Table S5, deviations from this simple octahedral-prismatic dichotomy occur. For non-oxido vanadium(IV) complexes, the absence of a strongly directional oxido ligand renders the d-orbital energies highly sensitive to subtle geometric distortions, variations in donor and π-bonding properties, and metal–ligand covalency. Even nominally trigonal-prismatic structures may therefore stabilize a predominantly d_{z^2}-type SOMO and exhibit a *g*-tensor with prolate character, while distorted octahedral geometries may acquire increasing *e′* character and shift towards oblate anisotropy. Thus, while the general correlation between coordination geometry and *g*-tensor anisotropy provides a useful qualitative framework for non-oxido vanadium(IV) systems, the experimentally observed exceptions highlight the decisive role of the actual ground-state orbital composition in determining the magnetic response.

Because both the *g*- and *A*-tensor anisotropies originate from the same electronic ground state, their overall trends are expected to co-vary; however, since the *g* tensor reflects spin–orbit coupling pathways while the *A*-tensor is governed by the spatial distribution of the unpaired electron density at the metal center, their principal axes and anisotropy directions do not necessarily coincide. Together, they provide complementary information on the orientation and extent of the magnetic anisotropy. Moreover, the close similarity of the fitted *g*- and *A*-tensors for **1** and **2** further suggests that their coordination environments in frozen solution differ only subtly from those established crystallographically, indicating that both complexes retain their characteristic ligand-field asymmetry upon vitrification.

In this context, it is worth noting that previous studies have suggested that in non-oxido vanadium(IV) complexes a general qualitative trend exists between the largest component of the hyperfine coupling tensor *A* and the angular descriptor *Ω*, defined as the donor–V–donor angle between the terminal donor atoms of the two tridentate ligands, with larger *A* values corresponding to increasing *Ω*.[39,47] According to this classification, all currently known non-oxido vanadium(IV) complexes with tridentate hydrazone-based ligands exhibit so-called type-3 spectra, with *A* values falling in the range from 340–400 MHz (113–135 × 10^4 cm^{-1}) and corresponding *Ω* values between 125 and 160°. In this qualitative correlation such type-3 spectra have been associated with structures intermediate between octahedral and trigonal-prismatic geometries. Although the angular descriptor *Ω* qualitatively accounts for the basic spectral appearance as far as the *A*-tensor anisotropy is concerned, *Θ* and the CShM parameters *S*(TRP-6) and *S*(OC-6) are better suited to describe structural variation in the series of literature-known non-oxido vanadium(IV) complexes with tridentate hydrazone-based ligands (*vide supra*) and are consistent with the observed *g*-tensor anisotropy (Table S5).

Relaxation times

The spin-relaxation properties of complexes **1** and **2** were studied in diluted frozen solutions. The temperature dependence of the spin–lattice relaxation times (T_1) was investigated by standard inversion-recovery experiments performed in the temperature range from 5–50 K (Fig. S7–S10). A maximum temperature of 50 K was used because the signal-to-noise ratio deteriorated significantly above this temperature. The resulting traces were fitted with an exponential decay function (see eqn (2)) and the temperature-dependent plot of the determined T_1 times is displayed in Fig. 4.

$$I = I_0 - A \exp\left(-\frac{T}{T_1}\right) \quad (2)$$

The T_1 values decrease steadily from approximately 110–150 ms at 5 K to about 35–43 μs at 50 K (Table S6). Furthermore, the T_1 values in protiated and deuterated solvents are almost indistinguishable, indicating that solvent vibrations play no discernible role in directing the spin–lattice relaxation, as also reported for related systems.[68] Since electron–nuclear coupling is reduced when protons are replaced by deuterons, the absence of a change in T_1 suggests that such

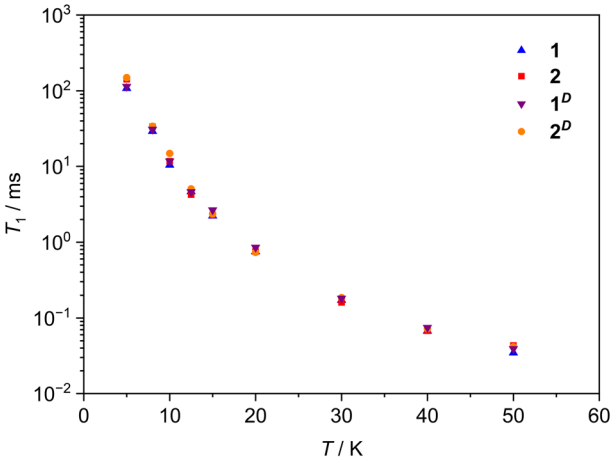

Fig. 4 Temperature dependence of T_1 times for complexes **1** and **2**, obtained from inversion-recovery measurements between 5 and 50 K in protiated (PhCl) and deuterated chlorobenzene (PhCl-d_5). Measurements in deuterated solvent are indicated by the superscript *D*.

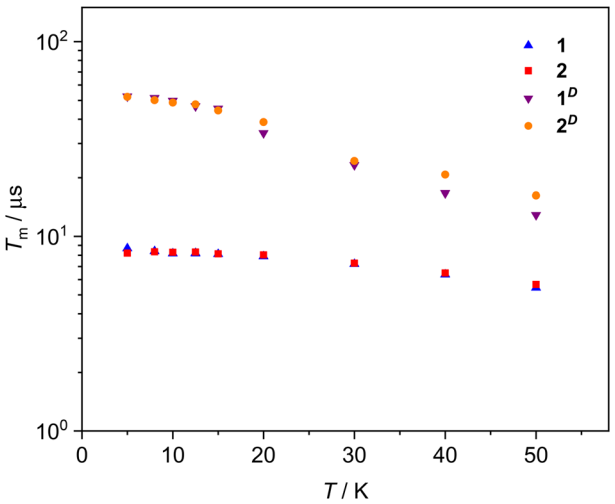

Fig. 5 Temperature dependence of T_m times for complexes **1** and **2**, obtained from Hahn-echo decay measurements between 5 and 50 K in protiated (PhCl) and deuterated chlorobenzene (PhCl-d_5). Measurements in deuterated solvent are indicated by the superscript *D*.

couplings do not noticeably affect the relaxation process.[69] No significant differences were observed between complexes **1** and **2**, indicating that the additional hydroxy group does not measurably influence the spin–lattice relaxation.

Assessment of the qubit properties of both complexes requires evaluation of their spin-coherence times. These were obtained using a Hahn-echo pulse sequence and monitoring the decay of the echo intensity to determine the phase-memory time (T_m; for details, see Experimental section). Measurements were performed between 5 and 50 K in frozen dilute solutions in protiated and deuterated chlorobenzene at an applied field of 347 mT (Fig. S11–S14), corresponding to the maximum echo intensity in the EDFS ESR spectra (Fig. S6). No limitations due to spin–lattice relaxation (T_1) were observed across the investigated temperature range. The decay traces were fitted with a stretched exponential according to eqn (3) and the results are summarized in Table S7.

$$I = I_0 - A \exp\left[-\left(\frac{2\tau}{T_m}\right)^{\beta}\right] \quad (3)$$

The decay curves of **1** and **2** recorded in protiated chlorobenzene (PhCl) show pronounced oscillations, attributed to electron spin-echo envelope modulation (ESEEM) from nearby protons (Fig. S15). For both complexes, the T_m values range between 5 and 8 µs at low temperatures and remain almost constant up to approximately 20 K, where they begin to decrease moderately. The weak temperature dependence below 20 K is consistent with nuclear spin diffusion.[19]

Repeating the measurements in deuterated chlorobenzene (PhCl-d_5) resulted in a substantial increase in T_m, reaching approximately 52 µs at 5 K (Fig. 5 and Table S7). This is consistent with the reduction of electron–nuclear coupling upon substitution of protons with deuterons in the solvent.[70] Because deuterium has a smaller magnetic moment than protium, its coupling to the electron spin is weaker, thus reducing decoherence and leading to significantly increased T_m values.[71]

Above 5 K, the differences between the T_m values of the two complexes are minor, independent of whether protiated or deuterated solvent is used. This is rationalized by noting that the additional hydroxy group in **2** lies within the nuclear spin-diffusion barrier determined for ^{1}H nuclei in similar systems and therefore does not contribute significantly to decoherence.[12,72]

Below approximately 15 K, the decay rates exhibit only a weak temperature dependence. In protiated solvent, this behavior is consistent with nuclear spin diffusion driven by the surrounding ^{1}H bath. In deuterated solvent, the dominant proton reservoir is removed and nuclear spin diffusion is therefore strongly suppressed. The remaining protons located within the spin-diffusion barrier do not contribute to decoherence, as they are too strongly coupled to undergo mutual flip-flops. Above about 15 K, the gradual decrease in T_m likely reflects the onset of thermally activated molecular motions that increasingly facilitate decoherence.

Coherent spin control

To assess the suitability of the present systems as molecular qubits, echo-detected transient nutation experiments were performed at variable microwave power. Representative nutation traces for complex **2**, recorded in protiated chlorobenzene, are shown in Fig. 6, together with their corresponding Fourier transforms. Analogous measurements for **1** as well as for deuterated solvent are provided in Fig. S16–S18.

Clear Rabi oscillations are observed for both complexes in protiated and deuterated solvent, demonstrating coherent manipulation of the electron spin. The extracted Rabi frequencies (Ω_R) increase linearly with the applied microwave field

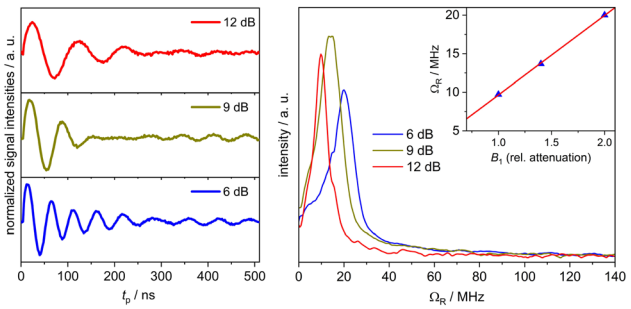

Fig. 6 Echo-detected transient nutation measurements for complex **2** in protiated chlorobenzene (PhCl, 0.1 mM) at 5 K. Left: Rabi oscillations recorded at different microwave attenuation levels. Right: Fourier-transformed spectra yielding the corresponding Rabi frequencies; the inset shows the linear dependence of the Rabi frequency on the applied microwave field strength.

strength (consistent with $\Omega_R \propto B_1$), as summarized in Fig. 6, confirming genuine nutation behavior. At intermediate power (9 dB attenuation), Rabi frequencies in the range of 13 MHz are obtained (Table S8).

The performance of molecular spin qubits is commonly benchmarked by the product between Rabi frequency and phase-memory time, FoM = $\Omega_R T_m$,[18,71,73] which reflects the number of coherent spin rotations executable within the coherence window. This metric has been widely adopted in the molecular qubit literature as a practical figure of merit for quantum control and qubit operability. The obtained FoM values for complexes **1** and **2** amount to 157 and 174 for the protiated samples and increase to 1016 and 1024 in deuterated solvent. The pronounced enhancement upon deuteration demonstrates that decoherence is predominantly governed by the surrounding nuclear spin bath rather than intrinsic electronic spin–spin interactions. These results position the present vanadium(IV) complexes among competitive candidates for molecular spin qubits in frozen solution.

Spin-bath analysis using CCE simulations

To further elucidate the dominant decoherence mechanism, cluster correlation expansion (CCE)[56] simulations were performed using the PyCCE package.[57] Following an approach similar to that reported in ref. 58, the central spin was placed either in a nuclear spin bath (hydrogen/deuterium, density 2×10^{22} cm^{-3}) or in an electronic-spin bath of variable concentration. The simulated coherence time T_2 is expected to approximate the experimentally determined phase-memory time T_m under dilution-limit conditions, where decoherence is governed predominantly be spin-bath interactions.

For a proton bath, the calculated coherence time amounts to approximately 8 μs, whereas substitution by deuterium increases the coherence time by nearly one order of magnitude, in qualitative agreement with the experimental findings (Fig. 5 and Table S7). In contrast, electron–spin-induced decoherence becomes relevant only at elevated spin concentrations. As shown in Fig. 7, the simulated coherence time decreases

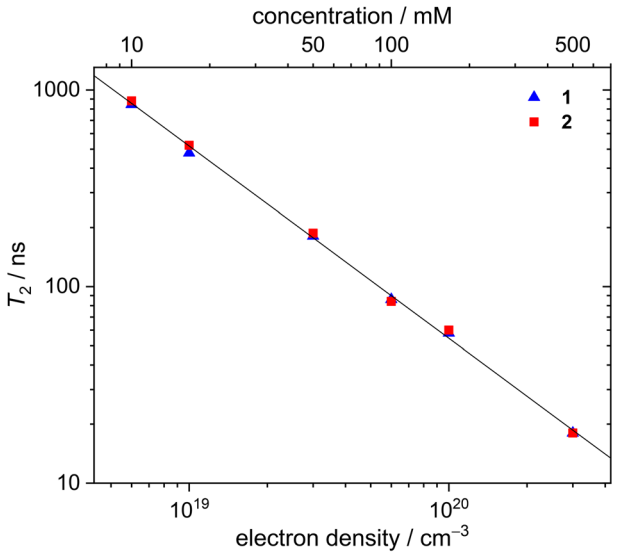

Fig. 7 Simulated coherence time T_2 as a function of electron–spin density in the surrounding bath for complexes **1** (blue triangles) and **2** (red squares), obtained from CCE calculations. Both axes are shown on a logarithmic scale. The black solid line represent a global linear fit to all data points, used to estimate the concentration at which electron–spin-induced decoherence becomes comparable to nuclear–spin-induced decoherence.

systematically with increasing electron density. The crossover between nuclear- and electron–spin-dominated decoherence is estimated to occur at approximately 6×10^{17} cm^{-3} (≈1 mM), consistent with earlier findings by Lunghi *et al.* for the complex [VO(TPP)].[58] Since the experimental concentration (0.1 mM) lies well below this threshold, the present systems are considered to operate in the dilution limit, where decoherence is dominated by the surrounding nuclear spin bath.

Electron spin-echo envelope modulation spectra

To further characterize possible interactions of the electron spin with nuclear spins other than the hosting ^{51}V nucleus, three-pulse electron spin-echo envelope modulation (ESEEM) experiments were performed on both **1** and **2** in protiated and deuterated chlorobenzene. The resulting time-domain data were Fourier transformed into the frequency domain, and the corresponding spectra are depicted in Fig. 8.

The fact that all but one signal disappear upon switching to a deuterated solvent leads to the conclusion that the vanishing features originate from hyperfine interactions with ^{1}H nuclei of the surrounding solvent shell.[74] Given that this shell is not sharply defined, the appearance of multiple broadened signals is reasonable. The sharp peak remaining in the spectra recorded in deuterated solvent is attributed to hyperfine interaction with the ^{14}N nuclei of the ligand (2.32 MHz),[75,76] which are located well within the assumed spin-diffusion barrier. Additional weak features may arise from couplings to protons in the ligand backbone. However, further discrimination is not possible based on the available data.

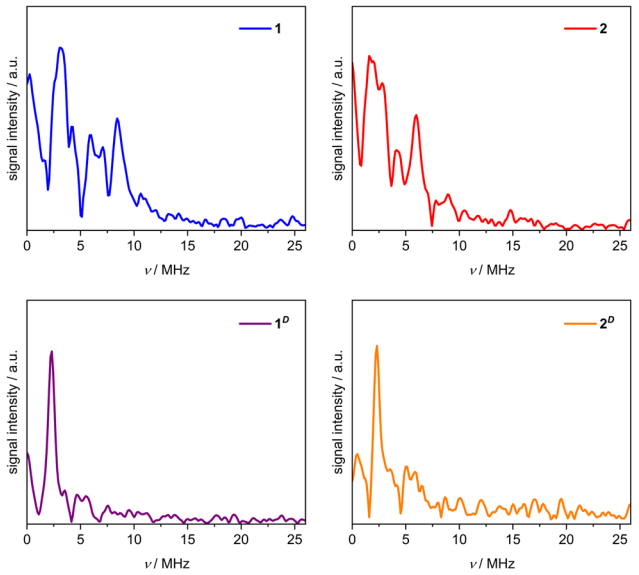

Fig. 8 Fourier-transformed (frequency-domain) ESEEM spectra of **1** (left) and **2** (right) recorded in protiated (top) and deuterated chlorobenzene (bottom) at 10 K.

Conclusions

The two chemically related new non-oxido vanadium(IV) complexes **1** and **2** show only minor differences in their six-coordinate geometries in the solid state. Echo-detected field-swept (EDFS) ESR measurements in chlorobenzene reveal that these structural distinctions largely vanish in solution, indicating that they arise mainly from packing effects rather than intrinsic electronic or steric features of the ligands. The ESR-derived parameters are consistent with a distorted coordination environment intermediate between the octahedral and trigonal-prismatic limits.

Both complexes exhibit non-limiting T_1 relaxation and long T_m times at low temperatures, which are further enhanced in deuterated solvent, highlighting their favorable spin-dynamic properties. Coherent control of the electron spin was demonstrated by pronounced Rabi oscillations with high figures of merit, confirming the suitability of these systems for qubit applications.

Comparative T_m and ESEEM data clearly demonstrate that decoherence is governed predominantly by interactions with the protonic solvent environment rather than with protons intrinsic to the complexes. Cluster correlation expansion (CCE) simulations quantitatively support these findings and show that, under the applied dilution conditions, nuclear–spin-driven decoherence prevails, whereas electron–spin-induced contributions would become significant only at substantially higher concentrations.

The presence of a peripheral hydroxy group in **2**, which rigidifies the ligand backbone and introduces an additional proton-bearing site, does not significantly influence either relaxation or coherence properties compared with **1**. This suggests that functionalization at this position—for example to enable controlled surface attachment—can be achieved without compromising qubit-relevant spin dynamics. Further enhancement of coherence times is therefore anticipated upon immobilization on surfaces, where the solvent spin bath is effectively removed.

Conflicts of interest

There are no conflicts to declare.

Data availability

Additional data supporting this article have been included in the supplementary information (SI). Supplementary information: literature survey of T_m times of vanadium(IV) complexes, thermogravimetric data, structural details, ESR spectral data from EDFS, T_1, and T_m measurements, Rabi oscillation measurements, and spin-bath analysis using CCE simulations. See DOI: https://doi.org/10.1039/d5dt02909k.

CCDC 2506301 (**1**) and 2506302 (**2**) contain the supplementary crystallographic data for this paper.[77a,b]

Acknowledgements

The authors would like to thank Jakob Meyer for his help with the experiments during his internship. S. L. is thankful to the DAAD for the support by a scholarship (Ref. No. 91769177). The purchase of ESR equipment was enabled by the Deutsche Forschungsgemeinschaft (DFG, German Research Foundation, project number INST 275/406-1 FUGG) and the state of Thuringia. R. D. thanks SERB [Grant No. CRG/2023/000884], and also CSIR, Govt. of India [Grant No. 01(3073)/21/EMR-II] for funding.

References

1 T. D. Ladd, F. Jelezko, R. Laflamme, Y. Nakamura, C. Monroe and J. L. O'Brien, *Nature*, 2010, **464**, 45–53.
2 A. Barenco, C. H. Bennett, R. Cleve, D. P. DiVincenzo, N. Margolus, P. Shor, T. Sleator, J. A. Smolin and H. Weinfurter, *Phys. Rev. A*, 1995, **52**, 3457–3467.
3 (*a*) R. Hanson and D. D. Awschalom, *Nature*, 2008, **453**, 1043–1049; (*b*) D. D. Awschalom, L. C. Bassett, A. S. Dzurak, E. L. Hu and J. R. Petta, *Science*, 2013, **339**, 1174–1179.
4 D. Loss and D. P. DiVincenzo, *Phys. Rev. A*, 1998, **57**, 120–126.
5 (*a*) S. Nakazawa, S. Nishida, T. Ise, T. Yoshino, N. Mori, R. D. Rahimi, K. Sato, Y. Morita, K. Toyota, S. Daisuke, S. M. Kitagawa, H. Hara, P. Carl, P. Höfer and T. Takui, *Angew. Chem., Int. Ed.*, 2012, **51**, 9860–9864; (*b*) D. Schäfter, J. Wischnat, L. Tesi, J. A. D. Sousa, E. Little, J. McGuire,

M. Mas-Torrent, C. Rovira, J. Veciana, F. Tuna, N. Crivillers and J. van Slageren, *Adv. Mater.*, 2023, **35**, 2302114.

6 (*a*) A. Zecevic, G. R. Eaton, S. S. Eaton and M. Lindgren, *Mol. Phys.*, 1998, **95**, 1255–1263; (*b*) E. R. Canarie, S. M. Jahn and S. Stoll, *J. Phys. Chem. Lett.*, 2020, **11**, 3396–3400; (*c*) S. M. Jahn, E. R. Canarie and S. Stoll, *J. Phys. Chem. Lett.*, 2022, **13**, 5474–5479.

7 (*a*) J. McGuire, H. N. Miras, J. P. Donahue, E. Richards and S. Sproules, *Chem. – Eur. J.*, 2018, **24**, 17598–17605; (*b*) J. McGuire, H. N. Miras, E. Richards and S. Sproules, *Chem. Sci.*, 2019, **10**, 1483–1491.

8 M. Atzori, L. Tesi, E. Morra, M. Chiesa, L. Sorace and R. Sessoli, *J. Am. Chem. Soc.*, 2016, **138**, 2154–2157.

9 L. Tesi, E. Lucaccini, I. Cimatti, M. Perfetti, M. Mannini, M. Atzori, E. Morra, M. Chies, A. Caneschi, L. Sorace and R. Sessoli, *Chem. Sci.*, 2016, **7**, 2074–2083.

10 C.-J. Yu, M. J. Graham, J. M. Zadrozny, J. Niklas, M. D. Krzyaniak, M. R. Wasielewski, O. G. Poluektov and D. E. Freedman, *J. Am. Chem. Soc.*, 2016, **138**, 14678–14685.

11 M. Atzori, E. Morra, L. Tesi, A. Albino, M. Chiesa, L. Sorace and R. Sessoli, *J. Am. Chem. Soc.*, 2016, **138**, 11234–11244.

12 M. J. Graham, C.-J. Yu, M. D. Krzyaniak, M. R. Wasielewski and D. E. Freedman, *J. Am. Chem. Soc.*, 2017, **139**, 3196–3201.

13 V. Lagostina, F. Carniato, D. Esteban-Gómez, C. Platas-Iglesias, M. Chiesa and M. Botta, *Inorg. Chem. Front.*, 2023, **10**, 1999–2013.

14 J. M. Zadrozny, J. Niklas, O. G. Poluektov and D. E. Freedman, *J. Am. Chem. Soc.*, 2014, **136**, 15841–15844.

15 C. E. Jackson, C.-Y. Lin, S. H. Johnson, J. van Tol and J. M. Zadrozny, *Chem. Sci.*, 2019, **10**, 8447–8454.

16 D. Stinghen, M. Atzori, C. M. Fernandes, R. R. Ribeiro, E. L. de Sá, D. F. Back, S. O. K. Giese, D. L. Hughes, G. G. Nunes, E. Morra, M. Chiesa, R. Sessoli and J. F. Soares, *Inorg. Chem.*, 2018, **57**, 11393–11403.

17 M. J. Graham, M. D. Krzyaniak, M. R. Wasielewski and D. E. Freedman, *Inorg. Chem.*, 2017, **56**, 8106–8113.

18 J. M. Zadrozny, J. Niklas, O. G. Poluektov and D. E. Freedman, *ACS Cent. Sci.*, 2015, **1**, 488–492.

19 G. R. Eaton and S. S. Eaton, *J. Magn. Reson.*, 1999, **136**, 63–68.

20 M. Atzori, S. Benci, E. Morra, L. Tesi, M. Chiesa, R. Torre, L. Sorace and R. Sessoli, *Inorg. Chem.*, 2018, **57**, 731–740.

21 M. Imperato, A. Nicolini, M. Boniburini, D. Sartini, E. Benassi, M. Chiesa, L. Gigli, Y.-K. Liao, A. Raza, E. Salvadori, L. Sorace and A. Cornia, *Inorg. Chem.*, 2024, **63**, 7912–7925.

22 M. Imperato, A. Nicolini, M. Borsari, M. Briganti, M. Chiesa, Y.-K. Liao, A. Ranieri, A. Raza, E. Salvadori, L. Sorace and A. Cornia, *Inorg. Chem. Front.*, 2024, **11**, 186–195.

23 (*a*) D. C. Crans, J. J. Smee, E. Gaidamauskas and L. Yang, *Chem. Rev.*, 2004, **104**, 849–902; (*b*) M. Sutradhar and A. J. L. Pombeiro, *Coord. Chem. Rev.*, 2014, **265**, 89–124; (*c*) M. R. Maurya, *Coord. Chem. Rev.*, 2019, **383**, 43–81.

24 (*a*) S. Roy, M. Böhme, S. Lima, M. Mohanty, A. Banerjee, A. Buchholz, W. Plass, S. Rathnam, I. Banerjee, W. Kaminsky and R. Dinda, *Eur. J. Inorg. Chem.*, 2022, e202200109; (*b*) I. Lippold, K. Vlay, H. Görls and W. Plass, *J. Inorg. Biochem.*, 2009, **103**, 480–486; (*c*) S. Nica, A. Buchholz, M. Rudolph, A. Schweitzer, M. Wächtler, H. Breitzke, G. Buntkowsky and W. Plass, *Eur. J. Inorg. Chem.*, 2008, 2350–2359; (*d*) I. Lippold, H. Görls and W. Plass, *Eur. J. Inorg. Chem.*, 2007, 1487–1491; (*e*) J. Becher, I. Seidel, W. Plass and D. Klemm, *Tetrahedron*, 2006, **62**, 5675–5681; (*f*) W. Plass and H.-P. Yozgatli, *Z. Anorg. Allg. Chem.*, 2003, **629**, 65–70; (*g*) W. Plass, *Eur. J. Inorg. Chem.*, 1998, 799–805; (*h*) W. Plass, *Z. Anorg. Allg. Chem.*, 1997, 461–477.

25 R. Dinda, E. Garribba, D. Sanna, D. C. Crans and J. Costa Pessoa, *Chem. Rev.*, 2025, **125**, 1468–1603.

26 (*a*) H. Kneifel and E. Bayer, *J. Am. Chem. Soc.*, 1986, **108**, 3075–3077; (*b*) R. E. Berry, E. M. Armstrong, R. L. Beddoes, D. Collison, S. N. Ertok, M. Helliwell and C. D. Garner, *Angew. Chem., Int. Ed.*, 1999, **38**, 795–797.

27 E. I. Stiefel, Z. Dori and H. B. Gray, *J. Am. Chem. Soc.*, 1967, **89**, 3353–3354.

28 (*a*) J. H. Welch, R. D. Beeman and P. Singh, *Inorg. Chem.*, 1988, **27**, 2862–2868; (*b*) W. E. Broderick, E. M. McGhee, M. R. Godfrey, B. M. Hoffmann and J. A. Ibers, *Inorg. Chem.*, 1989, **28**, 2902–2904; (*c*) M. Kondo, S. Minakoshi, K. Iwata, T. Shimizu, H. Matsuzaka, N. Kamigata and S. Kitagawa, *Chem. Lett.*, 1996, **25**, 489–490.

29 (*a*) S. R. Cooper, Y. B. Koh and K. N. Raymond, *J. Am. Chem. Soc.*, 1982, **104**, 5092–5102; (*b*) M. E. Cass, N. R. Gordon and C. G. Pierpont, *Inorg. Chem.*, 1986, **25**, 3962–3967; (*c*) T. W. Hambley, C. J. Hawkins and T. A. Kabanos, *Inorg. Chem.*, 1987, **26**, 3740–3745.

30 T. B. Karpishin, T. D. P. Stack and K. N. Raymond, *J. Am. Chem. Soc.*, 1993, **115**, 182–192.

31 P. Comba, L. M. Engelhardt, J. M. Harrowfield, G. A. Lawrance, L. L. Martin, A. M. Sargeson and A. H. White, *J. Chem. Soc., Chem. Commun.*, 1985, 174–176.

32 (*a*) T. A. Kabanos, A. M. Z. Slawin, D. J. Williams and J. D. Woollins, *J. Chem. Soc., Chem. Commun.*, 1990, 193–194; (*b*) U. Auerbach, B. P. C. D. Vedova, K. Wieghardt, B. Nuber and J. Weiss, *J. Chem. Soc., Chem. Commun.*, 1990, 1004–1006; (*c*) T. A. Kabanos, A. M. Z. Slawin, D. J. Williams and J. D. Woollins, *J. Chem. Soc., Dalton Trans.*, 1992, 1423–1427; (*d*) A. Neves, A. S. Ceccato, I. Vencato, Y. P. Mascarenhas and C. Erasmus-Buhr, *J. Chem. Soc., Chem. Commun.*, 1992, 652–654; (*e*) S. Bruni, A. Caneschi, F. Cariati, C. Delfs, A. Dei and D. Gatteschi, *J. Am. Chem. Soc.*, 1994, **116**, 1388–1394; (*f*) M. Farahbakhsh, H. Schmidt and D. Rehder, *Chem. Commun.*, 1998, 2009–2010.

33 (*a*) P. R. Klich, A. T. Daniher, P. R. Challen, D. B. McConville and W. J. Youngs, *Inorg. Chem.*, 1996, **35**, 347–356; (*b*) B.-S. Kang, X.-J. Wang, C.-Y. Su, H.-Q. Liu, T.-B. Wen and Q.-T. Liu, *Transition Met. Chem.*, 1999, **24**, 712–717.

34 (*a*) T. K. Paine, T. Weyhermüller, E. Bill, E. Bothe and P. Chaudhuri, *Eur. J. Inorg. Chem.*, 2003, 4299–4307; (*b*) T. K. Paine, T. Weyhermüller, L. D. Slep, F. Neese, E. Bill, E. Bothe, K. Wieghardt and P. Chaudhuri, *Inorg. Chem.*, 2004, **43**, 7324–7338.

35 (*a*) E. Ludwig, H. Hefele, E. Uhlemann, F. Weller and W. Kläui, *Z. Anorg. Allg. Chem.*, 1995, **621**, 23–28.

36 A. Diamantis, M. Manikas, M. Salam, M. Snow and E. R. T. Tiekink, *Aust. J. Chem.*, 1988, **41**, 453–468.

37 (*a*) W. Bansse, E. Ludwig, E. Uhlemann, F. Weller, K. Dehnicke and W. Herrmann, *Z. Anorg. Allg. Chem.*, 1992, **613**, 36–44; (*b*) Y. Jin and M. S. Lah, *Eur. J. Inorg. Chem.*, 2005, 4944–4952; (*c*) S. Gao, L.-H. Huo, H. Zhaoa and S. W. Ng, *Acta Crystallogr., Sect. E: Struct. Rep. Online*, 2005, **61**, m519–m521; (*d*) N. Biswas, D. Patra, B. Mondal, S. Bera, S. Acharyy, A. K. Biswas, T. K. Mukhopadhyay, A. Pal, M. G. B. Drewg and T. Ghosh, *Dalton Trans.*, 2017, **46**, 10963–10985; (*e*) N. Biswas, S. Bera, N. Sepay, A. Pal, T. Halder, S. Ray, S. Acharyy, A. K. Biswas, M. G. B. Drewg and T. Ghosh, *New J. Chem.*, 2020, **44**, 3700–3716.

38 (*a*) S. P. Dash, S. Pasayat, S. Bhakat, S. Roy, R. Dinda, E. R. T. Tiekink, S. Mukhopadhyay, S. K. Bhutia, M. R. Hardikar, B. N. Joshi, Y. P. Patil and M. Nethaji, *Inorg. Chem.*, 2013, **52**, 14096–14107; (*b*) S. P. Dash, S. Majumder, A. Banerjee, M. F. N. N. Carvalho, P. Adão, J. C. Pessoa, K. Brzezinski, E. Garribba, H. Reuter and R. Dinda, *Inorg. Chem.*, 2016, **55**, 1165–1182.

39 A. Banerjee, S. P. Dash, M. Mohanty, G. Sahu, G. Sciortino, E. Garribba, M. F. N. N. Carvalho, F. Marques, J. C. Pessoa, W. Kaminsky, K. Brzezinski and R. Dinda, *Inorg. Chem.*, 2020, **59**, 14042–14057.

40 (*a*) S. Kundu, D. Mondal, K. Bhattacharya, A. Endo, D. Sanna, E. Garribba and M. Chaudhury, *Inorg. Chem.*, 2015, **54**, 6203–6215; (*b*) A. Banerjee, S. A. Patra, G. Sahu, G. Sciortino, F. Pisanu, E. Garribba, M. F. N. Carvalho, I. Correia, J. Costa Pessoa, H. Reuter and R. Dinda, *Inorg. Chem.*, 2023, **62**, 7932–7953.

41 M. Sutradhar, G. Mukherjee, M. G. B. Drew and S. Ghosh, *Inorg. Chem.*, 2007, **46**, 5069–5075.

42 K. C. M. Westrup, T. Gregorio, D. Stinghen, D. M. Reis, P. B. Hitchcock, R. R. Ribeiro, A. Barison, D. F. Back, E. L. de Sa, G. G. Nunes and J. F. Soares, *Chem. Commun.*, 2011, **40**, 3198–3210.

43 T. Kajiwara, R. Wagner, E. Bill, T. Weyhermüller and P. Chaudhuri, *Dalton Trans.*, 2011, **40**, 12719–12726.

44 M. Kertesz and R. Hoffmann, *J. Am. Chem. Soc.*, 1984, **106**, 3453–3460.

45 B. Morgenstern, S. Steinhauser, K. Hegetschweiler, E. Garribba, G. Micera, D. Sanna and L. Nagy, *Inorg. Chem.*, 2004, **43**, 3116–3126.

46 L. Pisano, K. Várnagy, S. Timári, K. Hegetschweiler, G. Micera and E. Garribba, *Inorg. Chem.*, 2013, **52**, 5260–5272.

47 D. Sanna, G. Sciortino, V. Ugone, G. Micera and E. Garribba, *Inorg. Chem.*, 2016, **55**, 7373–7387.

48 B. V. Nonius, *COLLECT; Data Collection Software*, Delft, The Netherlands, 1998.

49 Z. Otwinowski and W. Minor, ch. Processing of X-ray Diffraction Data Collected in Oscillation Mode, in *Methods in Enzymology*, ed. C. W. Carter and R. M. Sweet, Academic Press, 1997, vol. 276, pp. 307–326.

50 *SADABS 2.10*, Bruker AXS Inc., Madison, Wisconsin, USA, 2002.

51 G. M. Sheldrick, *Acta Crystallogr., Sect. C: Struct. Chem.*, 2015, **71**, 3–8.

52 G. M. Sheldrick, *Acta Crystallogr., Sect. A: Found. Adv.*, 2015, **71**, 3–8.

53 H. Putz and K. Brandenburg, *Diamond - Crystal and Molecular Structure Visualization*, Bonn, Germany, https://www.crystalimpact.com/diamond.

54 *MATLAB version 24.2.0.2863752 (R2024b)*, The Mathworks, Inc., Natick, Massachusetts, 2024.

55 *OriginPro, Version 2024*, OriginLab Corporation, Northampton, MA, USA.

56 (*a*) W. Yang and R.-B. Liu, *Phys. Rev. B:Condens. Matter Mater. Phys.*, 2008, **78**, 085315; (*b*) W. Yang and R.-B. Liu, *Phys. Rev. B:Condens. Matter Mater. Phys.*, 2009, **79**, 115320.

57 M. Onizhuk and G. Galli, *Adv. Theory Simul.*, 2021, **4**, 2100254.

58 C. Ryan, V. Briganti, C. Hogan, M. O'Neill and A. Lunghi, *J. Chem. Phys.*, 2025, **163**, 134104.

59 (*a*) S. P. Dash, S. Roy, M. Mohanty, M. F. N. N. Carvalho, M. L. Kuznetsov, J. C. Pessoa, A. Kumar, Y. P. Patil, A. Crochet and R. Dinda, *Inorg. Chem.*, 2016, **55**, 8407–8421; (*b*) G. Sahu, A. Banerjee, R. Samanta, M. Mohanty, S. Lima, E. R. T. Tiekink and R. Dinda, *Inorg. Chem.*, 2021, **60**, 15291–15309.

60 (*a*) S. Nica, M. Rudolph, A. Buchholz, I. Lippold, H. Görls and W. Plass, *J. Inorg. Biochem.*, 2015, **147**, 193–203; (*b*) W. Plass, A. Pohlmann and H.-P. Yozgatli, *J. Inorg. Biochem.*, 2000, **80**, 181–183.

61 (*a*) W. Plass, *Inorg. Chim. Acta*, 1996, **244**, 221; (*b*) I. D. Brown and D. Altermatt, *Acta Crystallogr., Sect. B: Struct. Sci.*, 1985, **41**, 244–247.

62 M. Pinsky and D. Avnir, *Inorg. Chem.*, 1998, **37**, 5575–5582.

63 B. Morgenstern, B. Kutzky, C. Neis, S. Stucky, K. Hegetschweiler, E. Garribba and G. Micera, *Inorg. Chem.*, 2007, **46**, 3903–3915.

64 E. Lodyga-Chruscinska, A. Szebesczyk, D. Sanna, K. Hegetschweiler, G. Micera and E. Garribba, *Dalton Trans.*, 2013, **42**, 13404–13416.

65 (*a*) T. C. Baddeley, R. A. Howie, C. H. da Silva Lima, C. R. Kaiser, M. V. N. de Souza, J. L. Wardell and S. M. S. V. Wardell, *Z. Kristallogr.*, 2009, **224**, 506–514; (*b*) T. Xi-Shi and L. Peng-Fei, *Z. Kristallogr.*, 2018, **233**, 121–122.

66 (*a*) D. Plaul, A. Buchholz, H. Görls and W. Plass, *Polyhedron*, 2007, **26**, 4581–4590; (*b*) A. Roth, A. Buchholz, M. Gärtner, A. Malassa, H. Görls, G. Vaughan and W. Plass, *Z. Anorg. Allg. Chem.*, 2007, **633**, 2009–2018.

67 A. A. Diamantis, J. B. Raynor and P. H. Rieger, *J. Chem. Soc., Dalton Trans.*, 1980, 1731–1733.
68 K. Bader, M. Winkler and J. van Slageren, *Chem. Commun.*, 2016, **52**, 3623–3626.
69 J. Du, G. Eaton and S. Eaton, *J. Magn. Reson., Ser. A*, 1995, **115**, 213–221.
70 G. R. Eaton and S. S. Eaton, *Biol. Magn. Reson.*, 2002, **19**, 29–154.
71 A. Ardavan, O. Rival, J. J. L. Morton, S. J. Blundell, A. M. Tyryshkin, G. A. Timco and R. E. P. Winpenny, *Phys. Rev. Lett.*, 2007, **98**, 057201.
72 S. S. Eaton and G. R. Eaton, ch. Distance Measurements in Biological Systems by EPR, in *Biological Magnetic Resonance*, ed. L. J. Berliner, S. S. Eaton and G. R. Eaton, Klewer Academic/Plenum Publishers, New York, 2000, vol. 19, pp. 29–154.
73 M. Atzori and R. Sessoli, *J. Am. Chem. Soc.*, 2019, **141**, 11339–11352.
74 S. A. Cosgrove and D. J. Singel, *J. Phys. Chem.*, 1990, **94**, 8393–8396.
75 T. S. Smith, R. LoBrutto and V. L. Pecoraro, *Coord. Chem. Rev.*, 2002, **228**, 1–18.
76 S. S. Eaton, J. Dubach, K. M. More, G. R. Eaton, G. Thurman and D. R. Ambruso, *J. Biol. Chem.*, 1989, **264**, 4776–4781.
77 (*a*) CCDC 2506301: Experimental Crystal Structure Determination, 2026, DOI: 10.5517/ccdc.csd.cc2q40fb; (*b*) CCDC 2506302: Experimental Crystal Structure Determination, 2026, DOI: 10.5517/ccdc.csd.cc2q40gc.